PHYSICAL REVIEW B **97**, 014107 (2018)

Ab initio calculations of ideal strength and lattice instability in W-Ta and W-Re alloys

Chaoming Yang and Liang Qi
Department of Materials Science and Engineering, University of Michigan, Ann Arbor, Michigan 48109, USA

(Received 23 April 2017; revised manuscript received 1 January 2018; published 26 January 2018)

An important theoretical criterion to evaluate the ductility of metals with a body-centered cubic (bcc) lattice is the mechanical failure mode of their perfect crystals under tension along $\langle 100\rangle$ directions. When the tensile stress reaches the ideal tensile strength, the pure W crystal fails by a cleavage fracture along the $\{100\}$ plane so that it is intrinsically brittle. To discover the strategy to improve its ductility, we performed density functional theory and density functional perturbation theory calculations to study the ideal tensile strength and the lattice instability under $\langle 100\rangle$ tension for both W-Ta and W-Re alloys. Anisotropic linear elastic fracture mechanics (LEFM) theory and Rice's criterion were also applied to analyze the mechanical instability at the crack tip under $\langle 100\rangle$ tension based on the competition between cleavage propagation and dislocation emission. The results show that the intrinsic ductility can be achieved in both W-Ta and W-Re, however, by different mechanisms. Even though W-Ta alloys with low Ta concentrations are still intrinsically brittle, the intrinsic ductility of W-Ta alloys with high Ta concentrations is promoted by elastic shear instability before the cleavage failure. The intrinsic ductility of W-Re alloys is produced by unstable transverse phonon waves before the cleavage failure, and the corresponding phonon mode is related to the generation of $\frac{1}{2}\langle 111\rangle\{\bar{2}11\}$ dislocation in bcc crystals. The ideal tensile calculations, phonon analyses, and anisotropic LEFM examinations are mutually consistent in the evaluation of intrinsic ductility. These results bring us physical insights on the ductility-brittle mechanisms of W alloys under extreme stress conditions.

DOI: 10.1103/PhysRevB.97.014107

I. INTRODUCTION

As a refractory metal, tungsten (W) has the highest melting point of all pure metals and excellent high-temperature mechanical properties. It is a critical material in many engineering applications, such as fusion reactors and turbine engines. However, its formability and mechanical properties are severely limited by the room-temperature brittleness [1–5]. This poor ductility is related to the low dislocation mobility because a highly resolved shear stress is required to drive the dislocation motion at low temperature. Theoretical studies on dislocation behaviors of W and other similar refractory metals in a body-centered cubic (bcc) lattice revealed that the energetics of their dislocation motions are related to the filling of d valence electrons [6–10]. The extra d valence electrons in W alloys can enhance the double-kink nucleation of screw dislocations in a bcc lattice, which can increase dislocation mobility and result in solid solution softening, and decreasing d valence electrons lead to hardening and embrittlement [7,8].

To fully capture the essential mechanism of ductility, it is also necessary to analyze the competition between crack propagation and dislocation emission behaviors [11–17]. Both the crack propagation and dislocation emission can occur at the preexisting crack tip to release the strain energy by bond breaking and shear along stacking fault layers, respectively. A ductile material emits dislocations more efficiently at the crack tips and these dislocations blunt the crack to prevent the cleavage failure. The quantitative descriptions of these deformation defects depend on the geometry of crack tips and the external loading conditions. In this study, our objective is to connect the deformation defect behaviors to the inherent mechanical properties of W alloys. These inherent properties largely depend on the ideal strength behaviors, which describe the deformation and failure of perfect crystals under extreme stress without any influences of precursor defects [18,19]. From the stress perspective, the nucleation of specific deformation defects (dislocations and cracks) requires that the local stress reach the corresponding ideal tensile or shear strength [20,21].

First-principles calculations have been extensively used to investigate ideal tensile and shear strengths of different perfect crystals [18,19,22–25]. For single crystals of bcc metals such as W, the cleavage mostly occurs on the low-index $\{100\}$ plane, especially at relatively low temperatures [4,22,26–30], so their ideal tensile strengths under tension along $\langle 100\rangle$ directions have been well studied. Perfect crystals of the group-V transition metals vanadium (V) and niobium (Nb) fail by a shear deformation under the increasing $\langle 100\rangle$ tensile strain [23–25]. The tetragonal symmetry of the strained V or Nb crystal is broken into orthorhombic symmetry by a shear deformation as illustrated in Fig. 1 [the so-called *elastic shear instability* (ESI)], where the vectors $\mathbf{a}_2$ and $\mathbf{a}_3$ of the original cubic unit cell become nonperpendicular to each other. Thus, these materials prefer to shear plastic deformation, and they are intrinsically ductile. On the other hand, the strained bcc crystals are kept in tetragonal symmetry even when the tensile stress reaches the ideal tensile strength for both molybdenum (Mo) and W. These materials prefer to generate cleavage fracture along the $\{100\}$ plane, and they are intrinsically brittle [18,23,24].

Our recent studies [23] show that the intrinsic ductility can be achieved for Mo and W by alloying them with elements that have a lower number of valence electrons, such as Nb. When Nb concentration is beyond a critical value, ESI occurs to Mo-Nb alloys when the tensile stress reaches the ideal tensile strength, so Mo-Nb alloys become intrinsically ductile.

2469-9950/2018/97(1)/014107(14)

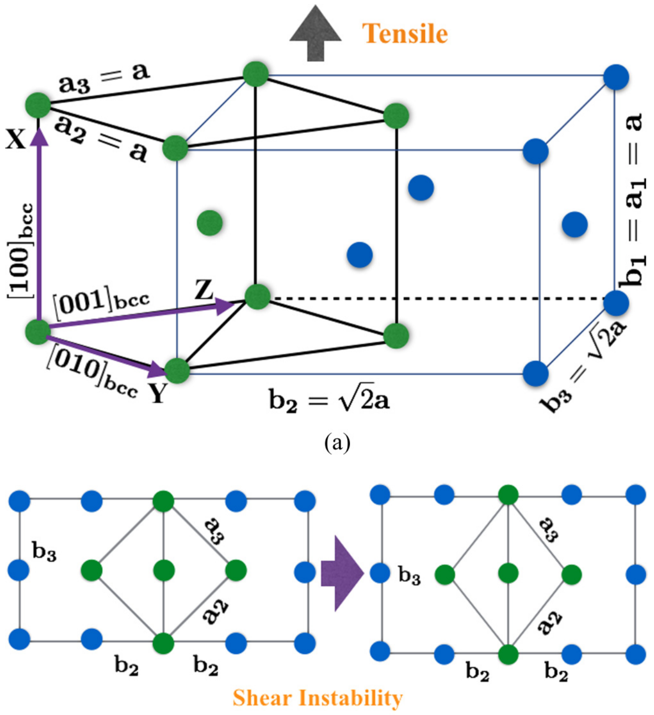

(a)

(b)

FIG. 1. (a) Two types of supercells of bcc crystals used in the ideal tensile calculations. The Cartesian coordinate system is defined along $\langle 100\rangle_{\text{bcc}}$. (b) Changes of the supercells due to elastic shear instability (ESI) under $[100]_{\text{bcc}}$ tensile strain viewed from the $[100]_{\text{bcc}}$ direction.

This transformation originates from the Jahn-Teller distortion effect depending on the electronic band filling level [31], where the tendency to break the symmetry of electronic band structures under the tensile strain is increased due to the downward shift of Fermi level. Oppositely, to increase valence electrons in Mo and W alloys can inhibit ESI and keep these alloys in intrinsically brittle status. This band filling effect is insensitive to specific characteristics of cations so that it can be implemented as a general strategy to improve the ductility of bcc refractory alloys.

However, it is well known that a certain amount of rhenium (Re) can substantially improve the ductility of W in engineering applications, and theoretical studies attribute these changes to the increase of dislocation mobility in W-Re alloys [2,7,8,32]. Since Re has one more valence electron than W, W-Re alloys should be intrinsically brittle according to the electronic band filling effect mentioned above [23,31]. Thus, there must be other possible mechanisms to reconcile the controversy between the prediction of intrinsic ductility based on electronic structures and the experimental observations.

The above inconsistency on the intrinsic ductility of W-Re alloys could be resolved by analyses of phonon dispersion relations of W alloys under mechanical deformation. ESI illustrated in Fig. 1 is a specific example of *elastic instability*, which means that the perfect crystal always deforms and transforms homogeneously until it becomes unstable under the applied tensile/shear stress equal to the ideal tensile/shear strength. On the other hand, unstable phonon modes with imaginary frequencies can emerge before the elastic instability when the applied load increases. The propagations of these unstable phonon modes generate different displacements for individual atoms and destroy the integrity of the perfect crystal. This phenomenon is called *phonon instability* [3,32,33]. It can be the initial step of either a transformation to another energetically favorable structure or the nucleation of a deformation defect (crack, dislocation, or deformation twin) [34,35]. Either elastic instability or phonon instability is a particular case of lattice instabilities, and there is a comprehensive review on lattice instabilities in metals [21].

The intrinsic ductility of a material can also be evaluated by the linear elastic fracture mechanics (LEFM) analyses [12]. The critical stress intensity factor for cleavage fracture propagation near a crack tip can be predicted by using elastic constants and surface energies of cleavage planes based on Griffith theory [36]. The critical stress intensity factor for dislocation emission near the crack tip can be predicted by using elastic constants and unstable stacking fault energies γ_{usf} of specific slip systems based on Rice theory [12]. The intrinsic ductility of this material can be determined based on the ratio between these two types of stress intensity factors [12,17]. These approaches have been examined and modified in cooperation with many atomistic simulations based on empirical interatomic potentials or first-principles calculations for different materials [14,15,17,37–41], including bcc metals [12,13].

In this paper, ideal tensile strengths and lattice instabilities of W, W-Ta, and W-Re alloys under [100] tensile strain are investigated by first-principles calculations based on density functional theory (DFT). W alloys are simulated by using both the standard superlattice method and the virtual crystal approximation (VCA) method [2,32]. The results show that additions of Ta can result in either intrinsically brittle or ductile behaviors of W-Ta alloys depending on Ta concentrations. Additions of Re can inhibit ESI for W-Re alloys. However, once Re concentration is above a critical value, transverse phonon modes with imaginary frequencies emerge for W-Re alloys before the elastic instability is reached under increasing tensile strain. These phonon instability phenomena correspond to dislocation nucleation events and make W-Re alloys intrinsically ductile. Additionally, LEFM analyses provide consistent results with the ideal tensile and phonon instability calculations of W-Ta and W-Re alloys. The details of the calculation methods are described in in Sec. II. The discussions on the results and the conclusions are explained in Secs. III and IV, respectively.

II. CALCULATION METHODS

A. Ideal tensile strength and phonon instability

The ideal tensile calculations were applied to different W alloy configurations. Pure W in the bcc lattice, WRe and WTa in the B2 structure, as well as $W_{15}Re_1$ and $W_{15}Ta_1$ in $2 \times 2 \times 2$ bcc supercells were investigated based on the standard pseudopotential for each chemical element. W_xTa_{1-x} and W_xRe_{1-x} ($x = 0.05$, 0.10, 0.15, 0.20, 0.25, and 0.50) alloys were investigated based on the pseudopotentials generated by the VCA method with the corresponding compositions. Two types of supercell structures employed in these calculations are illustrated in Fig. 1(a). One is the conventional bcc supercell composed by vectors $\mathbf{a}_{i=1,2,3}$, and it contains two atoms; the other is the tetragonal supercell composed by vectors $\mathbf{b}_{i=1,2,3}$, and it contains four atoms. The $[100]_{\text{bcc}}$ axis $\mathbf{a}_1$ in the bcc supercell is the same as [100] axis $\mathbf{b}_1$ in the tetragonal supercell. $\mathbf{b}_2$ and $\mathbf{b}_3$ in the tetragonal supercell are $[011]_{\text{bcc}}$ and $[0\bar{1}1]_{\text{bcc}}$, respectively.

An increasing tensile strain was applied along the [100] direction on two types of supercells in Fig. 1(a). In this paper, σ_{11} and $\varepsilon_{11} = (\frac{\mathbf{a}_1(\sigma_{11})}{\mathbf{a}_1(\sigma_{11}=0)} - 1.0)$ denote the true tensile stress and the engineering tensile strain along [100], respectively. In each quasistatic step of strain increment, $\varepsilon_{11} = 2.0\%$ was added along [100]; then the supercell was relaxed along other directions until all the stress tensor components $\sigma_{ij} < 0.05$ GPa except σ_{11}. During the supercell relaxations, the lengths along $\mathbf{a}_2 = [010]_{\text{bcc}}$ and $\mathbf{a}_3 = [001]_{\text{bcc}}$ of the bcc supercell in Fig. 1(a) were changed independently. Similarly, $\mathbf{b}_2 = [011]_{\text{bcc}}$ and $\mathbf{b}_2 = [0\bar{1}1]_{\text{bcc}}$ of the tetragonal supercell in Fig. 1(a) were also changed independently.

Two different deformation paths can be identified in the [100] ideal tensile calculations on these two types of supercells in Fig. 1(a). If the relaxed supercells under the fixed nonzero ε_{11} constraint always maintain tetragonal symmetry, the tensile deformation follows the tetragonal path (TP), where two types of supercells generate the same stress-strain (σ_{11}-ε_{11}) relations. However, a critical strain in the tetragonal supercell can lead to a structural transformation as shown in Fig. 1(b), where the original tetragonal supercell is transformed into an orthorhombic structure ($|\mathbf{b}_2| \neq |\mathbf{b}_3|$). So the tensile deformation follows the orthorhombic path (OP) and the elastic shear instability (ESI) may occur. TP and OP can cause different stress-strain relations. The ideal tensile strength σ_{11}^{IT} is the minimum value of σ_{11} to satisfy the condition of $\frac{d\sigma_{11}}{d\varepsilon_{11}} = 0$ along either of these two paths.

The phonon dispersion relations were calculated based on one-atom primitive cells for pure W and $\text{W}_x\text{Re}_{1-x}/\text{W}_x\text{Ta}_{1-x}$ alloys described in the VCA scheme. The lattice parameters of the primitive cells in phonon calculations were obtained by the above relaxation methods under fixed ε_{11} along TP. The wave vectors used in phonon calculations were along the paths following the selected high-symmetry points in the first Brillouin zone (FBZ) of the primitive cell. The coordinates of these high-symmetry points in reciprocal space are listed in Table I and plotted in Fig. 2 for primitive cells without and with the tensile deformation, respectively.

B. DFT calculation parameters

Density functional theory (DFT) calculations were performed by using the Vienna *Ab initio* Simulation Package (VASP) [42] and Quantum Espresso (QE) [43] in non-spin-polarized conditions. In VASP calculations, the applied pseudopotentials were based on the projector augmented wave (PAW) method [44] and the Perdew-Burke-Ernzerhof (PBE) exchange-correlation functional [45]. The k points were sampled using the Monkhorst-Pack method [46] by a $21 \times 21 \times 21$ grid for 2-atom bcc supercells, a $21 \times 19 \times 19$ grid for 4-atom tetragonal supercells, a $13 \times 13 \times 13$ grid for 16-atom bcc supercells, and a $13 \times 11 \times 11$ grid for 32-atom tetragonal supercells. The partial occupancies of each orbital were implemented in the first-order Methfessel-Paxton scheme with a smearing of 0.4 eV [47]. The kinetic cutoff energy was 380 eV. The program Phonopy [48] was employed to perform phonon spectrum calculations by the finite-displacement method (FDM) with the force constants from VASP calculations. The results of phonon calculations were used to analyze the atomic displacement modes of each phonon branch with imaginary frequencies.

TABLE I. Coordinates of the high-symmetry k points in the FBZ of bcc and bct (body-centered tetragonal) primitive cells shown in Fig. 2. The reciprocal coordinate is defined as the unit length equal to $\frac{2\pi}{|\mathbf{a}_{i=1,2,3}|}$. Here $\mathbf{a}_i$ as labeled in Fig. 1 can have different lengths due to the ideal tensile deformation.

bcc	bct	Reciprocal coordinates
N	N	[0.5 0.5 0]
H	SM	[0.0 0.5 0.0]
P	P	[0.5 0.5 0.5]
	GP	[0.5 0.25 −0.25]
Γ	Γ	[0 0 0]

In Quantum Espresso (QE) calculations [43], the virtual crystal approximation (VCA) scheme was employed to produce pseudopotentials of the virtual $\text{W}_x\text{Re}_{1-x}$ and $\text{W}_x\text{Ta}_{1-x}$ elements. These VCA pseudopotentials were generated by the Martins-Troullier (MT) approach [49] using the PBE exchange-correlation functional [50], and they were constructed by modifying the number of valence electrons per atom for the virtual chemical element using the program FHI98PP [51]. The k points were sampled using the Monkhorst-Pack method by a $25 \times 25 \times 25$ grid and a $25 \times 21 \times 21$ grid for the bcc and tetragonal supercells, respectively. The kinetic cutoff energy was 615 eV. Phonon dispersion curves and modes of atomic movements were calculated by the density functional perturbation theory (DFPT) [52], which was implemented by the Phonon packages of QE. An energy convergence threshold of 1×10^{-13} eV and a $6 \times 6 \times 6$ Monkhorst-Pack grid were used in DFPT calculations.

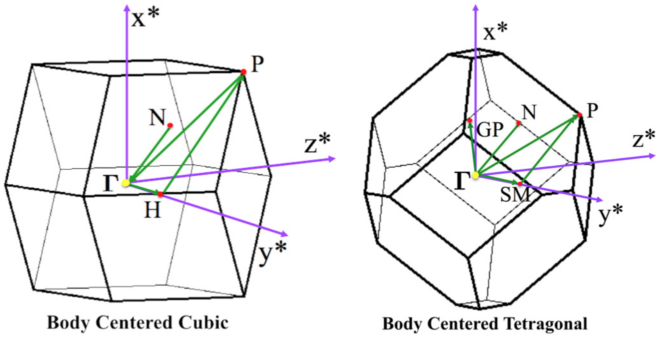

Body Centered Cubic
(a)

Body Centered Tetragonal
(b)

FIG. 2. (a) Paths (green lines) along high-symmetry points in the first Brillouin zone (FBZ) of bcc primitive cell for phonon calculations. (b) Changes of FBZ and the symmetric paths under $[100]_{\text{bcc}}$ tension along TP. The reciprocal coordinate system (x*-y*-z*) is defined based on the Cartesian coordinate system defined in Fig. 1(a).

C. Stacking fault and surface energies

A stacking fault is formed by shifting one part of a crystal relative to the rest along a slip vector on a slip plane [12,41,53]. The energy increment as a function of the slip vector is the generated stacking fault energy (GSF) or γ surface. The maximum energy increment along the minimum energy path (usually the same direction as the Burgers vector for bcc metals) of the γ surface is the unstable stacking fault energy γ_{usf}, which represents the energy barrier to shift two neighboring parts of the crystal on the slip plane.

DFT calculations were performed to obtain the γ surface in the Burgers vector direction $\langle 111\rangle$ of stacking fault planes $\{\bar{2}11\}$ and $\{\bar{1}10\}$ for pure W, $\mathrm{W}_x\mathrm{Ta}_{1-x}$, and $\mathrm{W}_x\mathrm{Re}_{1-x}$ alloys in the VCA scheme. The calculations were carried out by QE with the same VCA pseudopotentials applied in the ideal tensile calculations. The supercell geometry was $[\bar{1}11] \times [0\bar{1}1] \times [211]$ and $[\bar{1}11] \times [1\bar{1}2] \times [110]$ along the x-y-z axes with a periodicity of 1×1 on the x-y plane. The k points were sampled using the Monkhorst-Pack method by a $17 \times 9 \times 1$ grid and a $20 \times 7 \times 1$ grid in $\langle 111\rangle\{\bar{2}11\}$ and $\langle 111\rangle\{\bar{1}10\}$ γ surface calculations, respectively. Both types of supercells contained 12 layers of atoms and sufficient thickness of vacuum layers along the z axis. 25 evenly interpolated points were calculated along each slip path. The movement of atoms along the x and y directions on the slip plane was fixed for a given slip vector during the relaxation. The γ_{usf} was measured by the maximum GSF value along the slip path. Other parameters in DFT calculations were the same as those of the ideal tensile calculations.

Because the cleavage is mostly on the low-index $\{100\}$ planes for W [30], $\{100\}$ surface energies of pure W, $\mathrm{W}_x\mathrm{Ta}_{1-x}$, and $\mathrm{W}_x\mathrm{Re}_{1-x}$ alloys in the VCA scheme were calculated by DFT with the same VCA pseudopotentials for the further LEFM analyses based on Griffith theory [36]. The supercell geometry was $[100] \times [010] \times [001]$ along the x-y-z axis with the periodicity of 1×1 on the y-z plane. The supercells contained 14 layers of atoms and sufficient thickness of a vacuum layer along the x axis. The k points were sampled using the Monkhorst-Pack method by a $1 \times 16 \times 16$ grid. The energy relaxations were implemented by the conjugate gradient method in the DFT calculations. The $\{100\}$ surface energies were calculated based on the energies of supercells with or without the vacuum layer.

D. Linear elastic fracture mechanics

Anisotropic LEFM theory was applied to analyze the competition between crack propagation and dislocation emission on a semi-infinite crack in a homogeneous system [12,13,36,54]. A systematic summary of this method can be found in recent publications [16,17]. According to this method, the strain energy release rate G of the crack growth is

$$G = \mathbf{K}^T \Gamma \mathbf{K}. \tag{1}$$

$\mathbf{K}$ is the stress intensity factor given by

$$\mathbf{K} = [K_{\mathrm{I}}, K_{\mathrm{II}}, K_{\mathrm{III}}]^T, \tag{2}$$

where K_{I}, K_{II}, and K_{III} denote the stress intensity factors of the basic fracture modes I, II, and III, respectively. Γ is defined as

$$\Gamma = \tfrac{1}{2}\mathrm{Re}\{i\mathbf{A}\mathbf{B}^{-\mathbf{1}}\}, \tag{3}$$

where $\mathbf{A}$ and $\mathbf{B}$ originate from the eigenvectors of Stroh's formulas in solving defect problems for dislocations and cracks in a continuous medium under 2D plane strain conditions [54]. According to Griffith theory [36], the cleavage fracture happens when the strain energy release rate G equals the surface energy of the cleavage plane γ_{s}. The corresponding critical stress intensity factor $\mathbf{K}_{\mathrm{c}}$ is given by solving the equation

$$G_{\mathrm{c}} = \mathbf{K}_{\mathrm{c}}^T \Gamma \mathbf{K}_{\mathrm{c}} = 2\gamma_{\mathrm{s}}. \tag{4}$$

Rice analyzed the critical stress intensity factor $\mathbf{K}_{\mathrm{e}}$ for the dislocation nucleation and emission on the crack tip in isotropic elasticity [12]. Sun and Beltz [13] extended it to an anisotropic formula as

$$\mathbf{s}(\phi)\mathbf{K}^{\mathrm{eff}} = \sqrt{\gamma_{\mathrm{usf}}\Gamma_s(\theta,\phi)}. \tag{5}$$

K^{eff} is the effective stress intensity factor defined by the equation [12]

$$\mathbf{K}^{\mathrm{eff}} = \mathbf{F}(\theta)\mathbf{K}_{\mathrm{e}}, \tag{6}$$

where $\mathbf{F}(\theta)$ represents the angular-related matrix in the stress function of the crack tip resolved in a given slip plane. Thus, the critical stress intensity of dislocation emission is obtained by solving Eq. (6). Details of this formula were reviewed by Wu and Curtin [16]. Here γ_{usf} is the unstable stacking fault energy; ϕ is the angle between the Burgers vector and the crack front orientation projected to the slip plane; θ is the angle between the cleavage plane and the dislocation slip plane. $\mathbf{s}(\phi)$ is the slip vector based on the constrained path approximation [12] given by

$$\mathbf{s}(\phi) = (\cos\phi, 0, \sin\phi).$$

$\Gamma_s(\phi,\theta)$ is the resolved Γ based on

$$\Gamma_s(\phi,\theta) = \mathbf{s}(\boldsymbol{\Omega}\boldsymbol{\Gamma}\boldsymbol{\Omega}^T)^{-1}\mathbf{s}^T, \tag{7}$$

where Ω is the rotation matrix

$$\boldsymbol{\Omega} = \begin{bmatrix} \cos\theta & \sin\theta & 0 \\ -\sin\theta & \cos\theta & 0 \\ 0 & 0 & 1 \end{bmatrix}. \tag{8}$$

For pure W, $\mathrm{W}_x\mathrm{Ta}_{1-x}$, and $\mathrm{W}_x\mathrm{Re}_{1-x}$ alloys in the VCA scheme, LEFM analyses were performed to calculate the critical stress intensity factors for the dislocation nucleation on $\frac{1}{2}\langle 111\rangle\{\bar{2}11\}/\frac{1}{2}\langle 111\rangle\{\bar{1}10\}$ slip systems and the cleavage propagation along the $\{100\}$ plane under mode I loading along the $[100]$ direction. Figure 3 describes the geometry setup of the crack tips and slip systems. A semi-infinite crack sits in the y-z plane, and its front is along the z direction. The $K_{\mathrm{I}}, K_{\mathrm{II}}, K_{\mathrm{III}}$ are defined in the $[100]$, $[01\bar{1}]$, and $[011]$ directions of the bcc crystal, respectively. The critical stress intensity factor K_{Ic} for the cleavage propagation was calculated by Eq. (4), and the critical stress intensity K_{Ie} for dislocation emission was calculated by Eq. (6). The parameters for W and $\mathrm{W}_x\mathrm{Ta}_{1-x}/\mathrm{W}_x\mathrm{Re}_{1-x}$ alloys (including elastic constants, γ_{s}, and γ_{usf}) were obtained by the DFT calculations described in Secs. II B and II C.

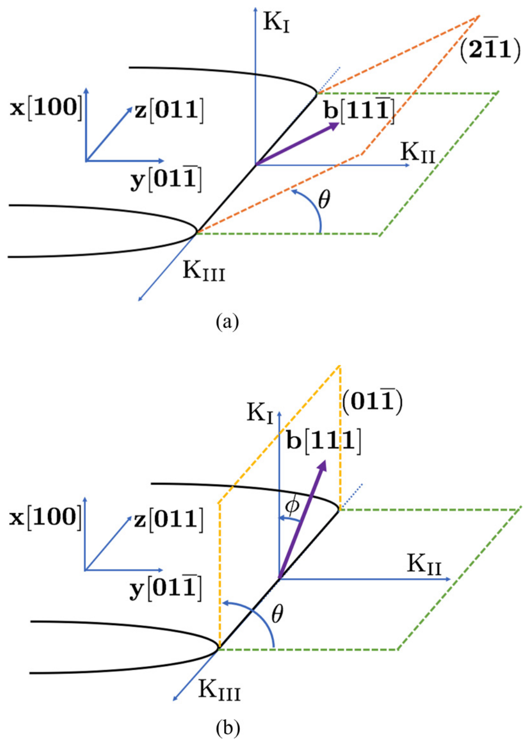

FIG. 3. Schematic diagram of the semi-infinite crack orientation and the dislocation slip system at the crack front for LEFM analyses. (a) $[11\bar{1}](2\bar{1}1)$ dislocation with $(\theta,\phi) = (54.73^\circ, 0.00^\circ)$; (b) $[111](01\bar{1})$ dislocation with $(\theta,\phi) = (90.00^\circ, 35.27^\circ)$, where θ and ϕ are defined in Eq. (5).

LEFM analyses are based on the energetic stability of possible dislocation nucleation events at the crack tip [12]. Figure 3 exhibits the potential dislocation slip systems that include the Burgers vector and the slip plane. However, there is no explicit limitation on the dislocation line directions in this 3-dimensional crystal. After the nucleation events, dislocation lines can propagate on the slip planes according to the strain field near the crack tip, and they can evolve to contain screw, edge, and mixed components with different values of dislocation mobility. Both these dislocation nucleation and propagation processes make significant contributions to improve the ductility of the material. To quantitatively evaluate their overall effects is beyond the scope of this study.

III. RESULTS AND DISCUSSION

A. Benchmarks

The structural and mechanical properties of pure W from this work and previous studies are summarized in Table II. The lattice constant a, bulk modulus B, and shear modulus C' [defined as $\frac{1}{2}(C_{11} - C_{12})$] obtained in this work are consistent with their counterparts from previous studies (the relative differences are no more than 5%). The ideal tensile strength $\sigma_{11}^{\rm IT}$ and the corresponding critical strain $\varepsilon_{11}^{\rm IT}$ along TP are also listed in Table II. The relative differences in $\sigma_{11}^{\rm IT}$ between our results and those from recent studies are no more than 3%. The phonon dispersion relations of pure W without strain from our benchmark calculations are plotted in Fig. 4. The FDM method using VASP and the DFPT method using QE show very similar phonon spectra along the sampled paths, and both of them are consistent with their counterparts from previous studies [3]. These results confirm that our calculations described in Secs. II B and II C are representative of the mechanical properties of perfect W crystals.

TABLE II. Lattice constant a (Å), bulk modulus B (GPa), shear modulus C' [$= \frac{1}{2}(C_{11} - C_{12})$] (GPa), the ideal tensile strength $\sigma_{11}^{\rm IT}$ (GPa), and the critical tensile strain $\varepsilon_{11}^{\rm IT}$ (%) for pure W from our calculations and previous studies.

	a	B	C'	$\varepsilon_{11}^{\rm IT}$	$\sigma_{11}^{\rm IT}$
VASP-PAW-PBE	3.171	284	164	14	29.6
QE-PBE	3.171	307.3	168	16	30.1
DFT-LDA [18]	3.17	331	161	13	29.5
FLAPW [22]				12.3	28.9
CPMD-PBE [19]	3.23	294		11.7	26.7
QE, VASP [2]	3.187, 3.189	300, 330	160, 159		
Exp. [55]	3.165	316	165		

Another concern arises about the validity of the VCA pseudopotentials in describing the mechanical properties of W-Re/W-Ta alloys. We first check the lattice constants and elastic properties calculated by using VCA pseudopotentials. The lattice constant, bulk modulus, C_{44}, and C' of the VCA $\mathrm{W}_x\mathrm{Ta}_{1-x}/\mathrm{W}_x\mathrm{Re}_{1-x}$ ($0.5 \leqslant x \leqslant 1.0$) alloys are summarized in Fig. 5, where the number of valence electrons per atom is determined by the alloy composition in the VCA scheme. For example, $\mathrm{W}_{0.50}\mathrm{Ta}_{0.50}$, W, and $\mathrm{W}_{0.50}\mathrm{Re}_{0.50}$ have 5.5, 6.0, and 6.5 valence electrons per atom, respectively. The lattice constant decreases and the bulk modulus increases with increasing valence electrons, consistent with the prediction based on the d-band filling and experimental measurements [55]. C_{44} monotonically increases with the addition of electrons, which agrees with the experiments as well [55]. Notably, the C' of W-Re alloys monotonically decreases with increasing d electrons, which manifests that the bcc W-Re alloy becomes structurally unstable due to the increment of Re concentration [55]. In summary, all these parameters change smoothly with the solid solute concentrations, and they coincide with the recent results of W-Ta/W-Re alloys using the VCA pseudopotentials [9]. So it is a reasonable approximation to apply these VCA

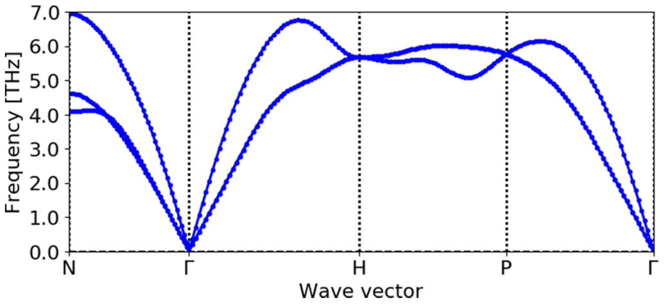

FIG. 4. The phonon dispersion relations of pure W along high-symmetry points of FBZ of the primitive unit cell calculated by the DFPT method using QE, which are consistent with results from the FDM method using VASP (these results are not shown here).

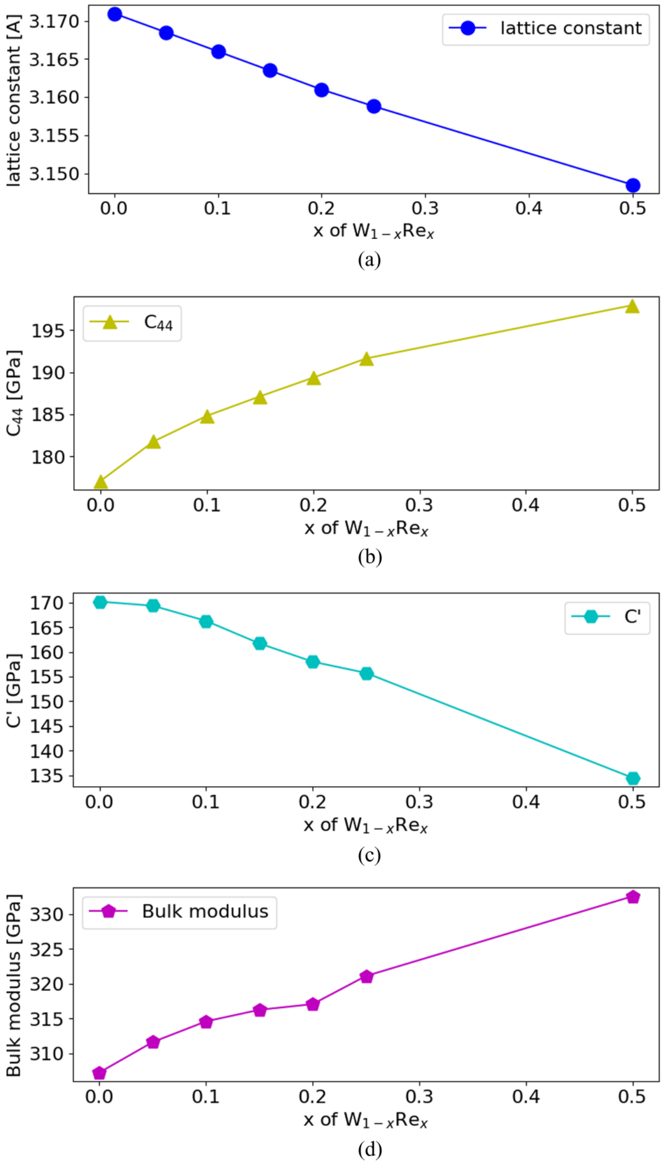

FIG. 5. The correlations of lattice constant (a), C_{44} (b), C' (c), and bulk modulus (d) with the concentration of Ta/Re in $W_{1-x}Ta_x/W_{1-x}Re_x$ in the VCA scheme, respectively. The number of valence electrons per atom is 5.0, 6.0, and 7.0 for pure Ta, W, and Re, respectively.

pseudopotentials to investigate the effects of Ta/Re solutes on the ideal strengths and lattice instability mechanisms of W alloys.

B. Ideal strength and shear instability

The ideal strength behaviors of W, W-Re, and W-Ta alloys were investigated based on different methods, including standard PAW-PBE pseudopotentials by VASP, standard MT-PBE pseudopotentials by QE, and VCA pseudopotentials by QE. All results are mutually consistent. Pure W exhibits intrinsically brittle behaviors because the elastic shear instability (ESI) along OP only occurs after the stress reaches the ideal tensile strength along TP. Alloying W with a large amount of Ta can generate intrinsically ductile behavior because fewer valence electrons promote ESI along OP before the stress reaches the ideal tensile strength along TP. Alloying W with Re can create ideal tensile behavior with more severe brittle characteristics because more valence electrons inhibit ESI along OP. More details are explained in the following.

1. *Ideal tensile strength of W-Ta alloys*

The ideal tensile behavior of W and W-Ta calculated by standard PAW-PBE pseudopotentials using VASP is summarized in Figs. 6(a) and 6(b). The stress-strain relations for pure W behave identically in both TP and OP when $\varepsilon_{11} < 18\%$ as shown in Fig. 6(a). In both TP and OP, σ_{11} reaches the ideal tensile strength $\sigma_{11}^{\mathrm{IT}} = 29.6$ GPa when ε_{11} reaches the ideal tensile strain $\varepsilon_{11}^{\mathrm{IT}} = 14\%$. When ε_{11} is larger than a critical value (nearly 18% for pure W), σ_{11} along OP drops dramatically compared with σ_{11} along TP. Above the same critical strain, the lattice constants of $\mathbf{b}_2$ along $[011]_{\mathrm{bcc}}$ and $\mathbf{b}_3$ along $[0\bar{1}1]_{\mathrm{bcc}}$ start to be divergent along OP as shown in Fig. 6(b). This transition of lattice constants is also described by ESI illustrated in Fig. 1(b). Thus, the critical strain for ESI, marked as $\varepsilon_{11}^{\mathrm{ESI}}$ in the following sections, is approximately 18%. However, such $\varepsilon_{11}^{\mathrm{ESI}}$ is at least 4% larger than $\varepsilon_{11}^{\mathrm{IT}}$ along TP. This means that the perfect W crystal should still fail by cleavage fracture deformation and pure W is intrinsically brittle.

Our recent investigations of ideal tensile behavior suggest that ESI is induced by the Jahn-Teller distortion of electronic structures [23]. The Jahn-Teller distortion splits the degenerate energy levels of symmetry-related and partially occupied electronic band structures near the Fermi level [56]. This distortion activates symmetry-breaking structural transformation and ESI along OP, so the reduction of valence electrons can shift down the Fermi level and induce ESI with smaller ε_{11} [23]. For alloy $W_{15}Ta_1$ in the conventional $2 \times 2 \times 2$ bcc supercell shown in Fig. 6(a), σ_{11} along TP and σ_{11} along OP are different when ε_{11} is above the critical strain 16%. In Fig. 6(b), lattice constants of $\mathbf{b}_2$ and $\mathbf{b}_3$ for $W_{15}Ta_1$ also become significantly divergent when ε_{11} is above 16%. So $\varepsilon_{11}^{\mathrm{ESI}}$ is 16% for $W_{15}Ta_1$. This confirms that a slight decrease in the number of valence electrons can induce ESI with smaller $\varepsilon_{11}^{\mathrm{ESI}}$ (16% for $W_{15}Ta_1$ vs 18% for pure W) [23]. However, because $\varepsilon_{11}^{\mathrm{ESI}}$ of $W_{15}Ta_1$ is still larger than $\varepsilon_{11}^{\mathrm{IT}} = 14\%$ corresponding to its $\sigma_{11}^{\mathrm{IT}}$ along TP shown in Fig. 6(a), $W_{15}Ta_1$ should still fail by cleavage mode along TP and it is intrinsically brittle. This is consistent with the recent study that shows W-Ta alloys are brittle when Ta concentration is small [9].

The number of valence electrons further decreases for WTa in the B2 structure. As shown in Fig. 6(a), the difference between σ_{11} along TP and σ_{11} along OP emerges when $\varepsilon_{11} >$ 14% for B2 WTa; its σ_{11} along OP reaches its $\sigma_{11}^{\mathrm{IT}}$ with the corresponding $\varepsilon_{11}^{\mathrm{IT}}$ at a certain value between 14% and 16%, since the σ_{11} has almost the same values at these two strain states. Meanwhile, $\sigma_{11}^{\mathrm{IT}}$ along TP can only be reached at $\varepsilon_{11}^{\mathrm{IT}} =$ 18%. In addition, the small divergence of lattice constants $\mathbf{b}_2$ and $\mathbf{b}_3$ for B2 WTa starts from $\varepsilon_{11} \sim 14\%$ and becomes evident when $\varepsilon_{11} = 16\%$ as shown in Fig. 6(b), indicating $\varepsilon_{11}^{\mathrm{ESI}}$ should be approximately 14%. Thus, WTa in the B2 structure should fail by ESI along OP and is intrinsically ductile. These results further confirm that the decrease of valence electrons in a group VI bcc transition metal can transform its mechanical properties

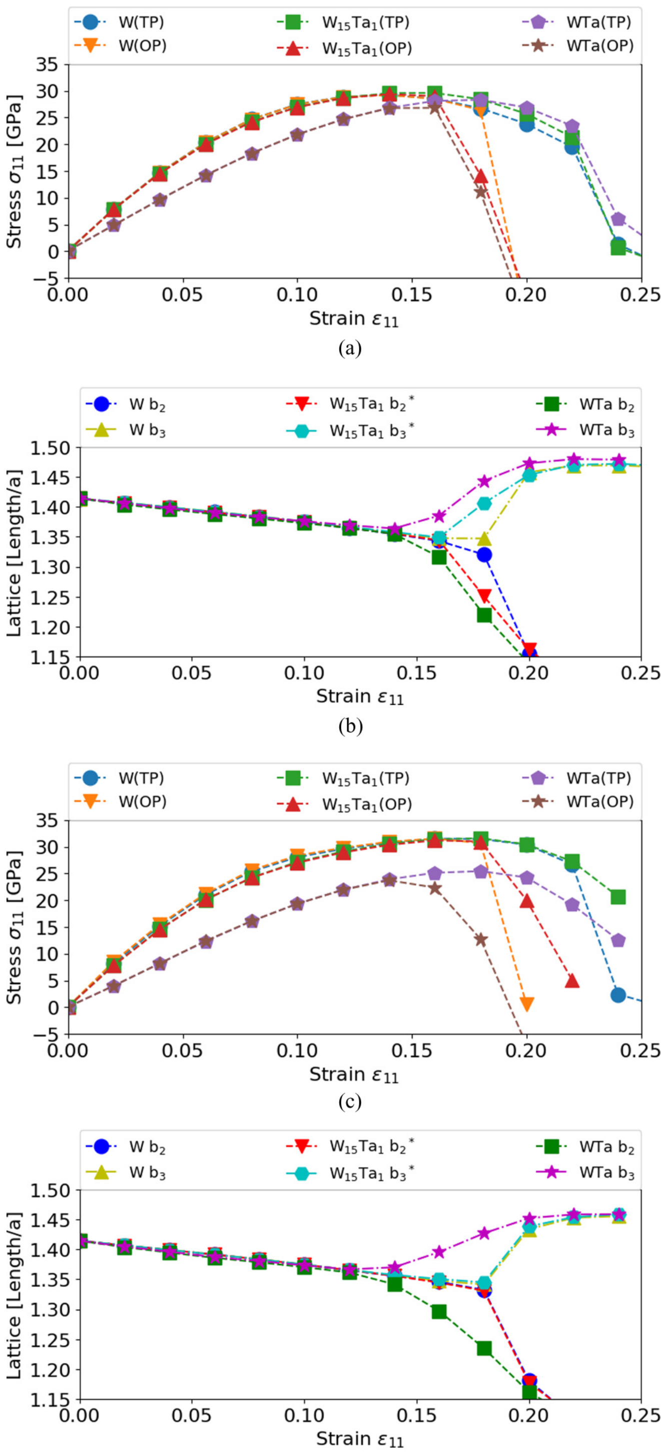

(a)

(b)

(c)

(d)

FIG. 6. The ideal tensile behavior of the perfect W and W-Ta alloys under [100] tensile strain. (a) and (c): The stress-strain curves along both the tetragonal path (TP) and orthorhombic path (OP) for pure W, $W_{15}Ta_1$ alloy, and B2 WTa alloy from VASP (a) and QE (c) calculations. (b) and (d): The corresponding variations of the lattice constants of the tetragonal supercells under [100] tensile strain along OP from VASP (a) and QE (c) calculations, respectively. Here $\mathbf{b}_2$ and $\mathbf{b}_3$ are defined in Fig. 1.

from intrinsically brittle to intrinsically ductile behavior under ideal tensile deformation [23].

All the above these calculations on W and W-Ta alloys are repeated by standard MT-PBE pseudopotentials using QE, and the results are plotted in Figs. 6(c) and 6(d). For pure W, the difference between σ_{11} along TP and σ_{11} along OP emerges when $\varepsilon_{11} > 18\%$. This critical strain is larger than $\varepsilon_{11}^{\rm IT} = 16\%$ for its $\sigma_{11}^{\rm IT}$ along TP, so it is still intrinsically brittle. For WTa in the B2 structure, ESI occurs at $\varepsilon_{11} = 14\%$ as illustrated by lattice constants $\mathbf{b}_2$ and $\mathbf{b}_3$ shown in Fig. 6(d). Correspondingly, σ_{11} reaches its $\sigma_{11}^{\rm IT}$ along OP at $\varepsilon_{11}^{\rm IT} = 14\%$, which is smaller than its counterpart $\varepsilon_{11}^{\rm IT} = 18\%$ along TP, so it is intrinsically ductile. These results are almost the same as those from VASP calculations with different types of pseudopotentials. This consistency provides strong evidence that the intrinsic brittle-to-ductile transition is the fundamental material property insensitive to calculation methods.

2. *Ideal tensile strength of W-Re alloys*

Our recent studies suggest that the addition of valence electrons into a group VI bcc transition metal inhibits its ESI along OP [23]. This prediction is confirmed by our current calculations of W-Re alloys by standard PAW-PBE pseudopotentials using VASP. Figure 7(a) shows $W_{15}Re_1$ at a slightly lower ideal tensile strength compared with pure W. σ_{11} along TP and σ_{11} along OP for $W_{15}Re_1$ are different when ε_{11} is above the critical strain 18%, similar to the case of pure W. At the critical strain $\varepsilon_{11} = 18\%$, the difference between $\mathbf{b}_2$ and $\mathbf{b}_3$ for $W_{15}Re_1$ is slightly smaller than its counterpart of pure W at the same strain, indicating less tendency for ESI for $W_{15}Re_1$. Such tendency is further enhanced as the Re concentration rises. For the B2 WRe alloy, TP and OP show the same stress-strain responses when $\varepsilon_{11} \leqslant 25\%$ as shown in Fig. 7(a), and the $|\mathbf{b}_2|$ and $|\mathbf{b}_3|$ always have the same values as shown in Fig. 7(b), indicating no ESI in the whole deformation path.

The calculations for W-Re alloys performed using standard MT-PBE pseudopotentials by QE provide essentially the same results as VASP calculations. When the Re concentration increases, the differences of σ_{11} between OP and TP decrease and vanish eventually as presented in Figs. 7(c) and 7(d). The supercell for the B2 WRe alloy keeps tetragonal symmetry throughout the deformation path, so it can completely inhibit ESI along OP due to the increment of the valence electrons.

The above calculations are based on the conventional supercells and standard pseudopotentials so that the ideal tensile behavior could be affected by the artificial order in supercells. The ideal tensile behavior and lattice constant variations of $W_{1-x}Re_x$ alloys based on the VCA pseudopotentials are presented in Fig. 8. These results contain no artificial-order effects so that they are more representative of the random binary solid solution alloys. When the concentration of Re increases from 10% ($W_{0.9}Re_{0.1}$) to 25% ($W_{0.75}Re_{0.25}$), the ideal tensile strength $\sigma_{11}^{\rm IT}$ decreases and the critical strain $\varepsilon_{11}^{\rm ESI}$, above which the stress and lattice constant divergences between the TP and OP emerge, increases from 18% to 20%. As Re concentration increases to 50% for $W_{0.5}Re_{0.5}$, $\sigma_{11}^{\rm IT}$ further decreases, and the two deformation paths become identical throughout the deformation path, the same as the B2 WRe alloy in Fig. 7. Because the VCA method ignores the variations of cation characteristics at different lattice sites, it further

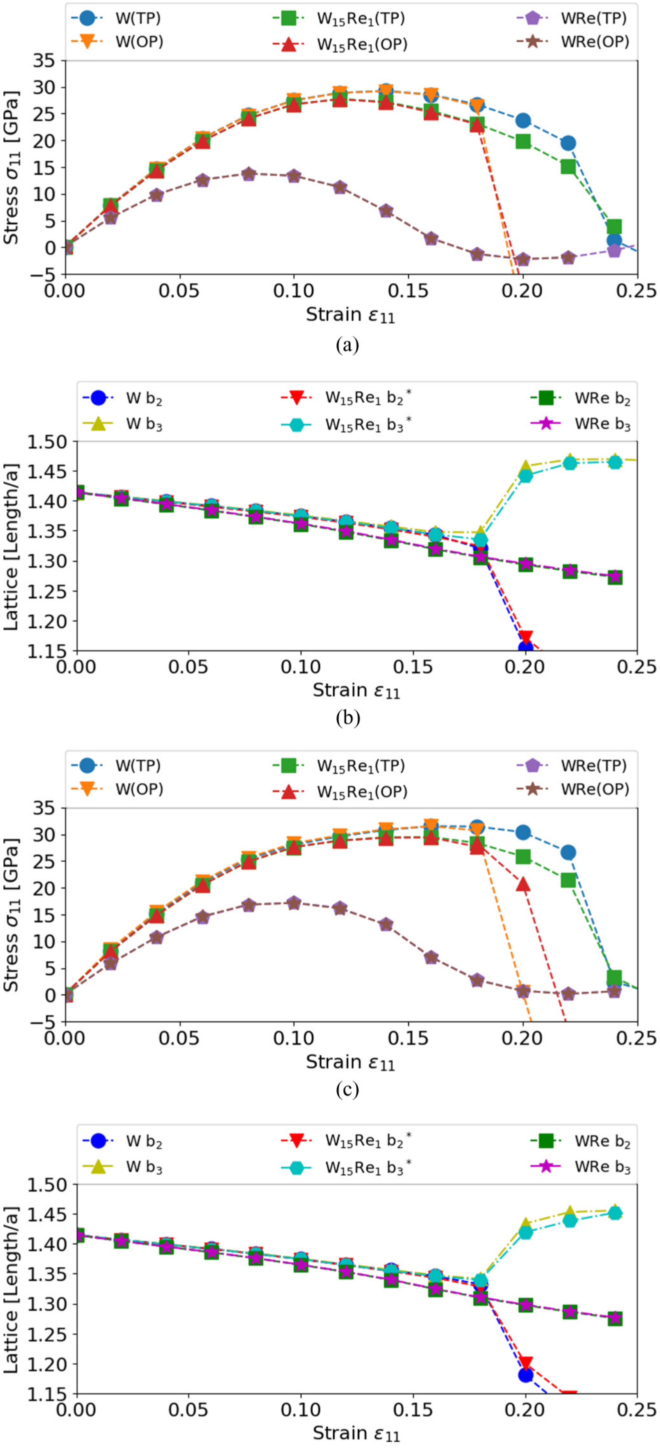

(a)

(b)

(c)

(d)

FIG. 7. The ideal tensile behavior of the perfect W and W-Re alloys under [100] tensile strain. (a) and (c): The stress-strain curves along both tetragonal path (TP) and orthorhombic path (OP) for pure W, $W_{15}Re_1$, alloy and B2 WRe alloy from VASP (a) and QE (c) calculations. (b) and (d): The corresponding variations of the lattice constants of the tetragonal supercells under [100] tensile strain along OP from VASP (a) and QE (c) calculations, respectively. Here $\mathbf{b}_2$ and $\mathbf{b}_3$ are defined in Fig. 1.

confirms that ESI along OP is inhibited for W-Re alloys mainly due to the *d*-band filling effect.

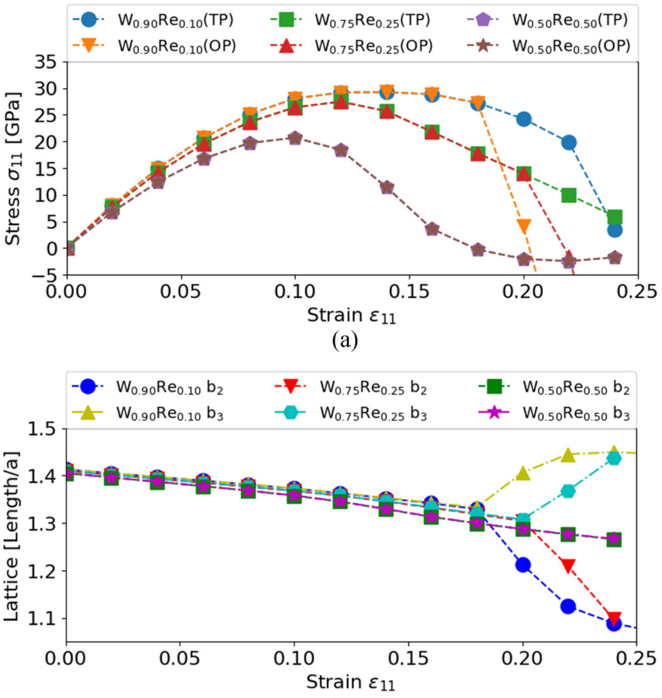

(a)

(b)

FIG. 8. The ideal tensile behavior of $W_{1-x}Re_x$ in the VCA scheme under [100] tensile strain. (a) Stress-strain curves along both tetragonal path (TP) and orthorhombic path (OP). (b) The corresponding variations of the lattice constants of the tetragonal supercells under [100] tensile strain along OP. Here $\mathbf{b}_2$ and $\mathbf{b}_3$ are defined in Fig. 1.

C. Ideal strength and phonon instability

According to Sec. III B, Re can inhibit ESI along OP and keep W-Re alloys in brittle failure mode under [100] ideal tensile deformation. This brittleness tendency is inconsistent with the experimental facts that the addition of Re can improve the ductility of W-based alloys [2,7,8,32]. However, the above investigations of W alloys only consider *elastic instability* (EI), which means the identical motion occurs to each atom of the crystal in a homogenous tensile or shear distortion until σ_{11} reaches $\sigma_{11}^{\mathrm{IT}}$ along either TP or OP. Besides, crystals can become dynamically unstable due to heterogeneous motions of atoms when there are imaginary frequencies for specific phonon modes, also called *phonon instability* (PI). Polarization vectors of these unstable phonon modes usually correspond to defect nucleation or structural transformation, such as dislocation emission or deformation twinning [34,35]. Therefore, analyses of phonon instability mechanisms for W, W-Ta, and W-Re alloys under [100] ideal tensile deformation are explained in this section.

1. Phonon instability in pure W

Figure 9 exhibits the evolution of phonon dispersion curves for pure W under increasing tensile strain along [100]. For a particular value of ε_{11}, only the phonon branch with the lowest frequencies of the phonon dispersion relations is plotted along a specific high-symmetry path in *k* space as defined in Fig. 2. By convention, imaginary frequencies are plotted as the negative values. Figure 9(a) exhibits that PI with imaginary

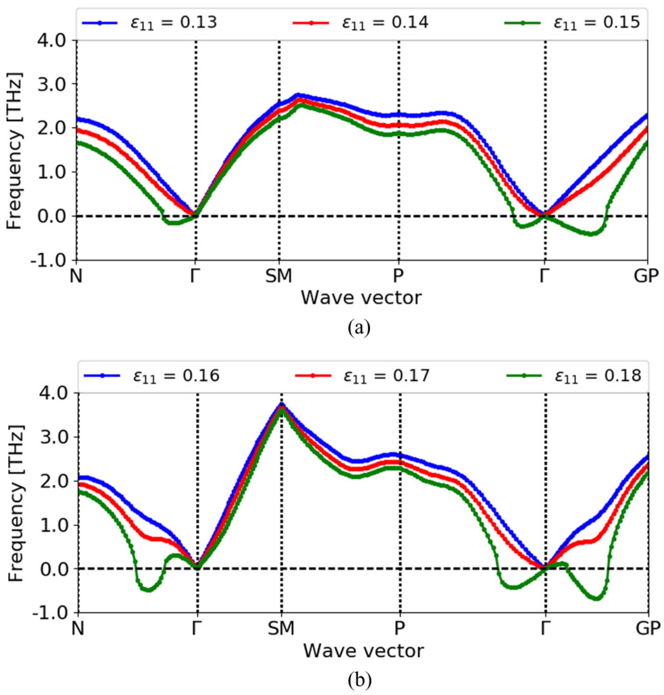

(a)

(b)

FIG. 9. Phonon frequencies of pure W under different ε_{11} along TP during the [100] ideal tensile deformation. Only the branches with the lowest frequencies of the phonon dispersion relations are plotted. (a) Phonon dispersion curves calculated by FDM methods using VASP. (b) Phonon dispersion curves calculated by DFPT method using QE.

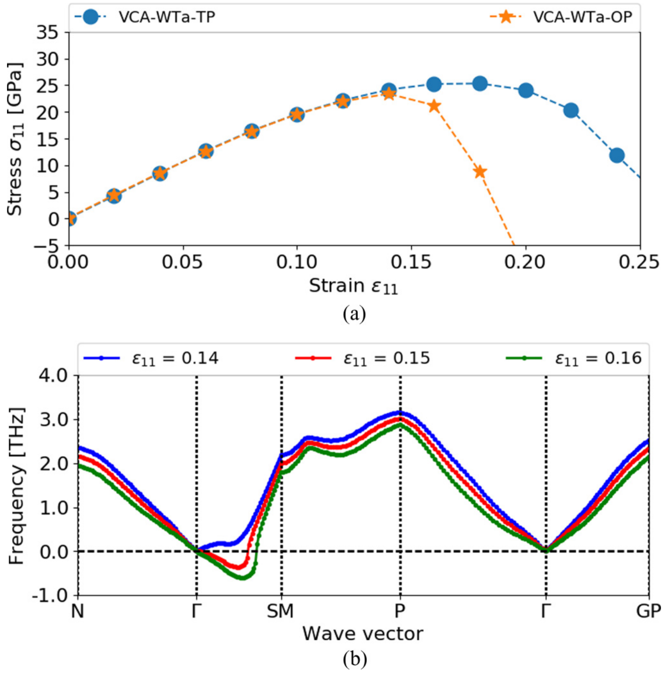

(a)

(b)

FIG. 10. (a) The ideal tensile behavior of $W_{0.5}Ta_{0.5}$ in the VCA scheme under [100] tensile strain. (b) Phonon frequencies of VCA $W_{0.5}Ta_{0.5}$ under different ε_{11} along TP during the [100] ideal tensile deformation calculated by DFPT method using QE. Only the branches with the lowest frequencies of the phonon dispersion relations are plotted.

frequencies is first observed near the Γ point at $\varepsilon_{11} = 15\%$ in the FDM calculations using VASP, but the critical strain $\varepsilon_{11}^{\mathrm{IT}} \approx 14\%$ for ideal tensile strength $\sigma_{11}^{\mathrm{IT}}$ along TP for pure W as shown in Fig. 6(a). In the DFPT calculations using QE, PI happens near the Γ point at $\varepsilon_{11} = 18\%$, and pure W also reaches $\sigma_{11}^{\mathrm{IT}}$ when $\varepsilon_{11} = 18\%$ along TP as shown in Fig. 6(c). If the critical ε_{11} for the appearance of PI under [100] ideal tensile deformation is defined as $\varepsilon_{11}^{\mathrm{PI}}$, it can be found as $\varepsilon_{11}^{\mathrm{PI}} = \sigma_{11}^{\mathrm{IT}}$ for pure W (the small mismatch should be the consequence of different discrete step sizes for strain increments in ideal tensile and phonon calculations). The wave vectors of unstable phonon modes at $\varepsilon_{11}^{\mathrm{PI}}$ are always located at the Γ point, corresponding to the limit of long-wavelength motions that are equivalent to the homogenous elastic deformation. Therefore, for pure W, the phonon modes only become dynamically unstable when the system reaches its elastic limit under the ideal tensile strength. The phonon analyses verify that it is the elastic instability that leads to the brittle fracture of W.

2. *Phonon instability in W-Ta alloys*

Phonon instability analyses during ideal tensile deformation are also conducted for W-Ta and W-Re alloys. Since the atomic mass and valence electron number of Re/Ta differ from those of W, the artificial order in the superlattice structures (B2 WTa/WRe or $W_{15}Ta_1/W_{15}Re_1$ in a conventional 2 × 2 × 2 bcc unit cell) may significantly underestimate $\varepsilon_{11}^{\mathrm{PI}}$, the critical strain for the phonon instability [35]. We have verified that $\varepsilon_{11}^{\mathrm{PI}}$ for the B2 WTa/WRe superlattice is indeed much smaller than $\varepsilon_{11}^{\mathrm{PI}}$ for VCA $W_{0.5}Ta_{0.5}/W_{0.5}Re_{0.5}$ (the results are not discussed in this paper). Such artificial ordering of the lattice structure usually does not exist in real W alloys. Therefore, only the phonon instability analyses applied to W alloys in the VCA scheme are discussed in the following sections.

For the VCA $W_{0.5}Ta_{0.5}$ alloy, the stress-strain behavior and the corresponding phonon dispersion curves are plotted in Fig. 10. The stress-strain behavior for the VCA $W_{0.5}Ta_{0.5}$ calculated by QE in Fig. 10(a) is almost equal to the results for B2 WTa calculated by VASP in Fig. 6(a) and those by QE in Fig. 6(c). The VCA $W_{0.5}Ta_{0.5}$ is also intrinsically ductile under the [100] tensile, since $\sigma_{11}^{\mathrm{IT}}$ is first obtained when ε_{11} increases to $\varepsilon_{11}^{\mathrm{IT}} \approx 14\%$ along OP before $\varepsilon_{11}^{\mathrm{IT}} \approx 18\%$ along TP. The DFPT method is applied to calculate the phonon dispersion relations of the VCA $W_{0.5}Ta_{0.5}$ using the primitive unit cell under an increasing ε_{11} along TP. Figure 10(b) shows that the Γ-*X* phonon branch along [0 ξ 0] first becomes negative near the Γ point when $\varepsilon_{11} \approx 15\%$, close to its $\varepsilon_{11}^{\mathrm{IT}}$ along OP (the small mismatch is the consequence of different discrete step sizes for strain increments in ideal tensile and phonon calculations). Thus, similarly to the case of pure W, the VCA $W_{0.5}Ta_{0.5}$ becomes dynamically unstable due to the phonon modes corresponding to the limit of long-wavelength motions when the system reaches its elastic limit under the ideal tensile strength.

Analyses of the polarization and wave vectors of the unstable phonon mode further confirm that the phonon instability in the VCA $W_{0.5}Ta_{0.5}$ is equivalent to elastic shear instability (ESI) along OP. The polarization vectors and wave vectors

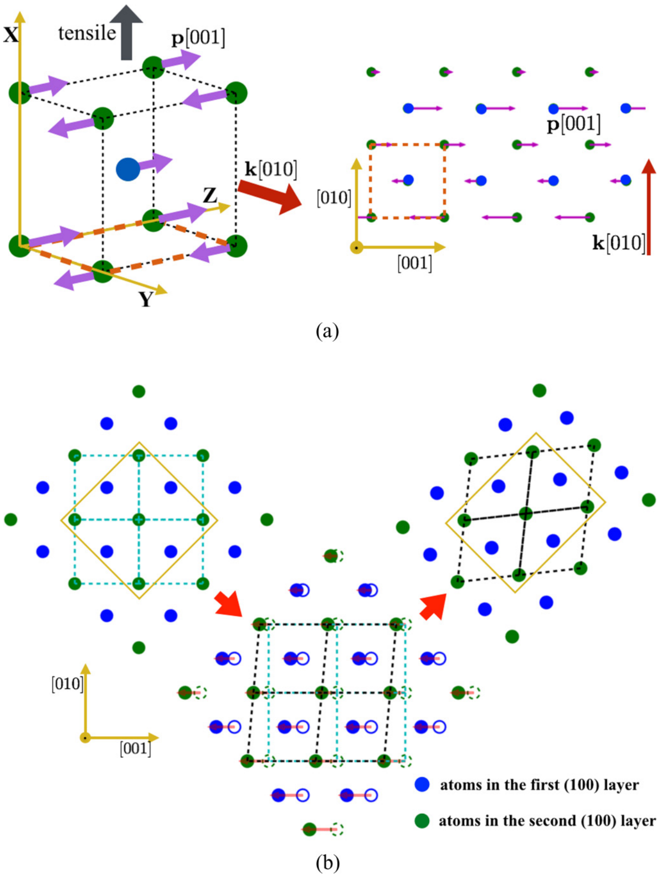

(a)

(b)

FIG. 11. A sketch of the unstable $T_{[001]}[0\ \xi\ 0]$ phonon mode in VCA $W_{0.5}Ta_{0.5}$ alloy. (a) The polarization vector **p** and the wave vector **k** of the unstable phonon mode. (b) Projection of the crystal structure on $(100)_{bcc}$ plane to illustrate that the consequence of phonon instability is equivalent to that of elastic shear instability in Fig. 1(b).

of the unstable phonon mode are plotted in Fig. 11(a). The wave vector **k** is along the [010] direction, and the polarization vector **p** is along the [001] direction. Since **k** is near the Γ point and perpendicular to **p**, the phonon has a long-wavelength transverse wave mode, denoted by $T_{[001]}[0\ \xi\ 0]$, and it should induce elastic shear deformation. In fact, the phonon mode $T_{[001]}[0\ \xi\ 0]$ near the Γ point is regarded as the elastic shear deformation that is closely related to the elastic constant C_{44} [3,33]. Figure 11(b) illustrates that the transverse waves of the $T_{[001]}[0\ \xi\ 0]$ mode shear the neighboring (010) atomic planes. As a result, one of the unit cell vectors ($[010]_{bcc}$ and $[001]_{bcc}$) in the 2D square lattice of the (100) plane is tilted relative to the other. This deformation geometrically transforms the 2D square lattice to a rhombus structure. Thus, the whole 3D lattice changes from the tetragonal to orthorhombic symmetry in the same ESI mechanism illustrated in Fig. 1(b) when the unstable phonon propagates.

3. Phonon instability in W-Re alloys

The phonon dispersion curves for VCA $W_{1-x}Re_x$ alloys under different ε_{11} during the [100] ideal tensile deformation are plotted in Fig. 12. For the VCA $W_{0.9}Re_{0.1}$ alloy in Fig. 12(a), the imaginary frequencies appear first near the Γ point when ε_{11} increases to the critical value $\varepsilon_{11}^{PI} = 15\%$, which is close to $\varepsilon_{11}^{IT} \approx 14\%$ for its ideal tensile strength σ_{11}^{IT} shown in Fig. 8(a). So this long-wavelength phonon instability is equivalent to its elastic instability, similarly to the case of pure W discussed in Sec. III C 1.

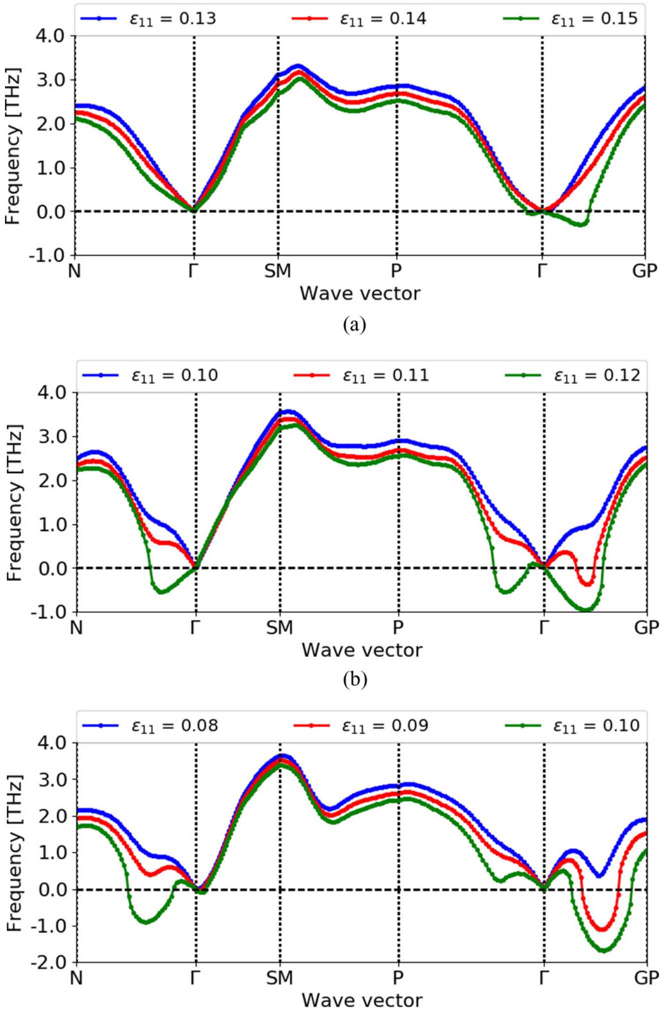

(a)

(b)

(c)

FIG. 12. Phonon frequencies of VCA $W_{1-x}Re_x$ under different ε_{11} along TP during the [100] ideal tensile deformation calculated by DFPT method using QE. (a) $W_{0.9}Re_{0.1}$. (b) $W_{0.75}Re_{0.25}$. (c) $W_{0.5}Re_{0.5}$. Only the branches with the lowest frequencies of the phonon dispersion relations are plotted.

For the VCA $W_{0.75}Re_{0.25}$ alloy in Fig. 12(b), the critical strain ε_{11}^{PI} for the emergence of imaginary frequencies is 11%, smaller than $\varepsilon_{11}^{IT} = 12\%$ for its σ_{11}^{IT} shown in Fig. 8(a), so the imaginary phonon frequencies appear before the stress reaches its σ_{11}^{IT} to induce the elastic tensile failure. Figure 12(b) also reveals that the unstable phonon modes are along the Γ-GP branch ($\mathbf{k} = [2\xi\ \xi\ \bar{\xi}]$) at the critical strain $\varepsilon_{11}^{PI} = 11\%$ for VCA $W_{0.75}Re_{0.25}$. Notably, when the phonon mode of the wave vector $\mathbf{k} = [0.2\ 0.1\ \overline{0.1}]$ along the Γ-GP branch first becomes negative (imaginary) at $\varepsilon_{11}^{PI} = 11\%$, other phonon branches, including long-wavelength modes near the Γ point, are still positive. This means that this phonon instability is not triggered by a long-wavelength phonon mode equivalent to

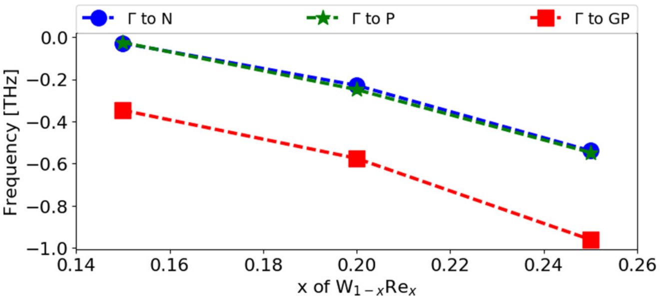

FIG. 13. The most negative phonon frequencies along different branches of phonon dispersion curves for different VCA $W_{1-x}Re_x$ alloys at $\varepsilon_{11} = 12\%$ during the [100] ideal tensile deformation.

homogenous elastic deformation. Instead, the crystal becomes dynamically unstable due to the phonon instability with a wavelength of several atomic layers. This short-wavelength phonon instability becomes further visible when the Re concentration increases. For the VCA $W_{50}Re_{50}$ alloy in Fig. 12(c), the imaginary phonon frequencies first appear at the critical strain $\varepsilon_{11}^{\mathrm{PI}} = 9\%$ before the stress reaches $\sigma_{11}^{\mathrm{IT}}$ at $\varepsilon_{11}^{\mathrm{IT}} = 10\%$ as shown in Fig. 8(a). The corresponding wave vector **k** is $[0.29\ 0.14\ \overline{0.14}]$ along the Γ-GP branch, also away from the Γ point.

The ideal tensile behavior and phonon spectrums of $W_{0.85}Re_{0.15}$, $W_{0.80}Re_{0.20}$, and $W_{0.75}Re_{0.25}$ alloys in the VCA scheme are also investigated to further confirm the effect of Re on the phonon instability of W-Re alloys. For all three of these compositions, the critical strain $\varepsilon_{11}^{\mathrm{IT}}$ corresponding to the ideal tensile strength $\sigma_{11}^{\mathrm{IT}}$ is close to 12%. Meanwhile, the most negative (imaginary) frequencies along different branches (Γ-N, Γ-P, and Γ-GP) as functions of Re concentration are plotted in Fig. 13. The figure reveals that the Γ-GP branch always has the most negative value for these alloys, suggesting that the first imaginary frequency always appears along the Γ-GP branch. With the increment of Re concentrations, the imaginary phonon modes always produce more negative frequencies. For example, the most negative frequency along the Γ-GP branch changes from ~ -0.4 THz for $W_{0.85}Re_{0.15}$ to ~ -1.0 THz for $W_{0.75}Re_{0.25}$, suggesting that the critical strain $\varepsilon_{11}^{\mathrm{PI}}$ for the emergence of imaginary frequencies should decrease with the increase of Re concentration. Thus, phonon instability along the Γ-GP branch for W-Re alloys is promoted by the increments of Re concentration and the number of valence electrons per atom.

Analyses of the polarization and wave vectors of the unstable phonon modes in the VCA $W_{0.75}Re_{0.25}$ alloy are illustrated in Fig. 14. When the critical strain of phonon instability $\varepsilon_{11}^{\mathrm{PI}}$ is applied, the unstable phonon propagates along the wave vector **k** perpendicular to the $(21\bar{1})$ planes, and atoms oscillate along the direction of the polarization vector **p** close to $[2\bar{1}1]$ with different phase factors. This unstable phonon mode can promote dislocation nucleations on the $\frac{1}{2}[1\bar{1}1](21\bar{1})$ slip system, which is among the most typical slip systems for bcc crystals. The angle between the polarization vector $\mathbf{p} \parallel [2\bar{1}1]$ and the Burgers vector $\frac{1}{2}[1\bar{1}1]$ is about 18°. This deviation between **p** and the Burgers vector is consistent with previous dynamic stability analyses [35], which indicate that the nucleation of a certain dislocation due to phonon instability requires the atoms on the potential slip plane to *roll over* their neighbor atoms to minimize the dislocation nucleation barrier. The phonon polarization direction **p** responds to the instantaneous *rolling* direction [35] as illustrated in Fig. 14(b). Thus, the unstable phonon for $W_{1-x}Re_x$ VCA alloys under the critical strain before the elastic tensile failure can activate the emission of $\frac{1}{2}\langle 111\rangle\{\bar{2}11\}$ dislocations and enhance the preference of ductile plastic deformation to the brittle fracture under extremely high stress conditions, such as the local region near the crack tip.

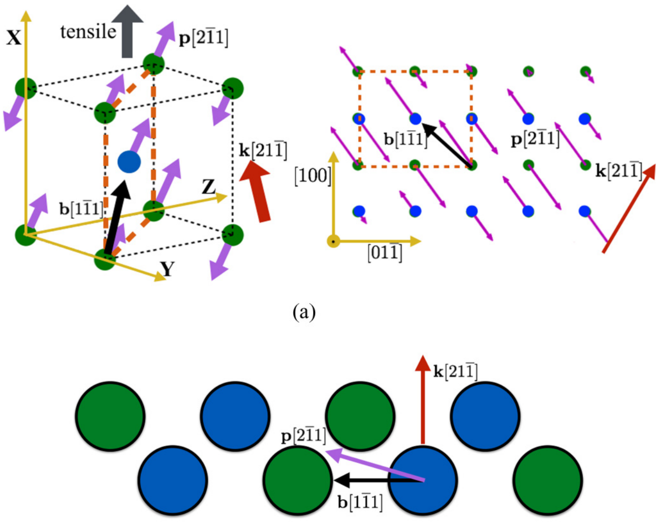

(a)

(b)

FIG. 14. A schematic illustration of the dynamic instability of $T_{[2\bar{1}1]}[2\xi\ \xi\ \bar{\xi}]$ phonon mode in VCA $W_{0.75}Re_{0.25}$ alloy. (a) The polarization vector **p** and the wave vector **k** of the unstable phonon mode shown in the 3D lattice (left) and on the projection of atoms on (011) plane (right). (b) Sketch of the hard-sphere "roll over" model [35]. The polarization vector **p** is the instantaneous tangent direction along the transition path of the dislocation nucleation event, and it has a small angle with Burgers vector *b*. Here the green/blue circles stand for atoms at the corner/center of bcc unit cells.

D. LEFM analyses

All the above studies of intrinsic brittleness/ductility are based on the ideal tensile behaviors of perfect crystals without the involvement of specific deformation defects. Results of linear elastic fracture mechanics formalism (LEFM) analyses are explained in this section to evaluate the intrinsic brittleness/ductility in the circumstances similarly to the deformation of real metals/alloys. These analyses output the critical stress intensity factors K_{Ic} for the cleavage propagation along the {100} plane and K_{Ie} for the emission of dislocations in the $\frac{1}{2}\langle 111\rangle\{\bar{2}11\}$ and $\frac{1}{2}\langle 111\rangle\{\bar{1}10\}$ slip systems for different $W_{1-x}Ta_x$ and $W_{1-x}Re_x$ VCA alloys under mode I loading along the ⟨100⟩ directions. The parameters in LFFM analyses listed in Table III are the elastic constants, surface energies $\gamma_{s\,(100)}$, and unstable stacking fault energies ($\gamma_{\mathrm{usf}\,(211)}$ and $\gamma_{\mathrm{usf}\,(110)}$) calculated using VCA pseudopotentials by QE. The results of K_{Ic} and K_{Ie} for different alloys are summarized in Fig. 15, where the number of valence electrons per atom

TABLE III. Parameters in LEFM analyses: lattice constant a (Å), elastic constants (GPa), and unstable stacking fault energy γ_{usf} and surface energy γ_s (J/m^2). The deviations between the values of pure W from our DFT calculations and those from previous results [57] should result from the usage of different pseudopotentials.

	a	C_{11}	C_{12}	C_{44}	$\gamma_{\mathrm{usf}\,(211)}$	$\gamma_{\mathrm{usf}\,(110)}$	$\gamma_{s\,(100)}$
$W_{0.50}Ta_{0.50}$	3.250	344	187	92	1.599	1.276	3.941
$W_{0.75}Ta_{0.25}$	3.209	436	189	123	2.182	1.859	4.65
$W_{0.80}Ta_{0.20}$	3.199	467	190	136	2.191	1.992	4.771
$W_{0.85}Ta_{0.15}$	3.189	487	191	148	2.241	2.083	4.862
$W_{0.90}Ta_{0.10}$	3.178	512	191	160	2.258	2.095	4.935
$W_{0.95}Ta_{0.05}$	3.172	532	193	170	2.245	2.133	4.992
W	3.171	534	193	177	2.120	2.021	4.847
W [57]	3.165	523	203	160	1.978	1.762	4.630
$W_{0.95}Re_{0.05}$	3.168	537	199	182	2.025	1.944	4.749
$W_{0.90}Re_{0.10}$	3.166	536	203	184	1.930	1.867	4.643
$W_{0.85}Re_{0.15}$	3.163	531	208	187	1.832	1.768	4.534
$W_{0.80}Re_{0.20}$	3.161	527	211	189	1.738	1.687	4.426
$W_{0.75}Re_{0.25}$	3.159	529	217	191	1.647	1.610	4.323
$W_{0.50}Re_{0.50}$	3.149	512	243	198	1.243	1.132	3.905

indicates the chemical composition of VCA $W_{1-x}Ta_x$ and $W_{1-x}Re_x$ alloys.

The individual values of K_{Ic} and K_{Ie} for $\frac{1}{2}\langle 111\rangle\{\bar{2}11\}$ and $\frac{1}{2}\langle 111\rangle\{\bar{1}10\}$ slip systems are plotted in Fig. 15(a). Starting from pure W (the number of valence electrons per atom equals 6.0), K_{Ic} and K_{Ie} of two slip systems both decrease with the increment of valence electrons per atom by adding more Re to W. These trends are consistent with the variations of $\gamma_{s\,(100)}$, $\gamma_{\mathrm{usf}\,(211)}$, and $\gamma_{\mathrm{usf}\,(110)}$ listed in Table III. A parameter $K_{\mathrm{Ie}}/K_{\mathrm{Ic}}$ is introduced to evaluate the intrinsic ductility of alloys because $K_{\mathrm{Ie}}/K_{\mathrm{Ic}}$ can quantitatively describe the preference of dislocation emission over the crack propagation to release the strain energy at the crack tip [12,17]. Figure 15(b) shows that $K_{\mathrm{Ie}}/K_{\mathrm{Ic}}$ decreases for both $\frac{1}{2}\langle 111\rangle\{\bar{2}11\}$ and $\frac{1}{2}\langle 111\rangle\{\bar{1}10\}$ slip systems when pure W is alloyed with higher Re concentrations in the VCA scheme. This means that increasing valence electrons in W promotes the dislocation emission near the crack tip under mode I loading along $\langle 100\rangle$ and leads to more ductile deformation. This result is consistent with above ideal tensile calculations, which show that alloying Re solutes can induce short-wavelength phonon instability for W alloys to raise the tendency of dislocation nucleation under the extremely high stress conditions.

Noticeably, $K_{\mathrm{Ie}}/K_{\mathrm{Ic}}$ of both $\frac{1}{2}\langle 111\rangle\{\bar{2}11\}$ and $\frac{1}{2}\langle 111\rangle\{\bar{1}10\}$ slip systems are larger than 1.0 for pure W. This means that the propagation of the $\{100\}$ cleavage fracture occurs under lower stress intensity factors than dislocation emissions at the crack tip under mode I loading described as Fig. 3, so pure W is intrinsically brittle. $K_{\mathrm{Ie}}/K_{\mathrm{Ic}}$ of $\frac{1}{2}\langle 111\rangle\{\bar{2}11\}$ becomes smaller than 1 when Re concentration is above a critical value slightly larger than 0.25 according to Fig. 15(b). This means that the $\frac{1}{2}\langle 111\rangle\{\bar{2}11\}$ dislocation emission occurs under lower stress intensity factors than the cleavage fracture, so $W_{1-x}Re_x$ VCA alloys are intrinsically ductile above this critical Re concentration [12,17]. Interestingly, this critical Re concentration is close to its counterpart to induce unstable phonon modes to activate dislocation nucleation before the elastic tensile failure predicted in Fig. 12(b).

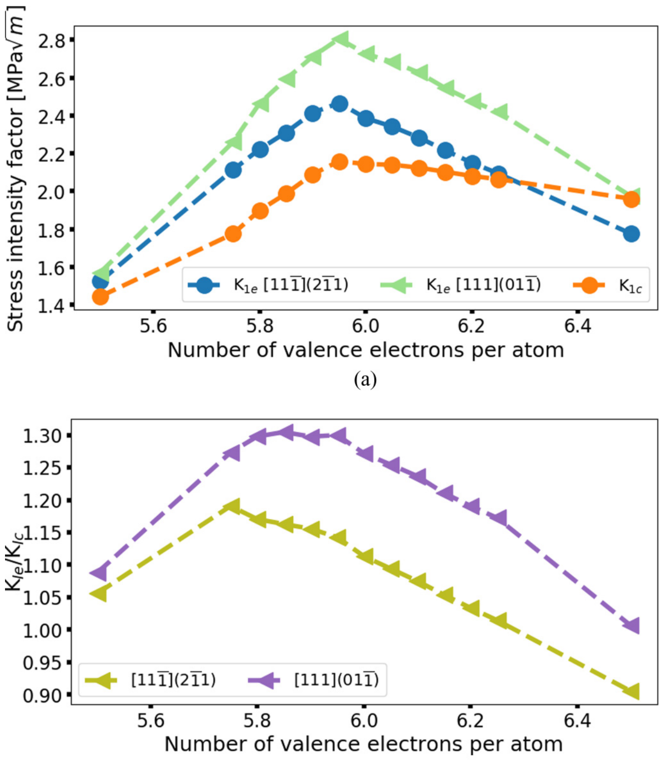

(a)
(b)

FIG. 15. Cleavage and dislocation emission competition for different W alloys in the VCA scheme predicted by anisotropic LEFM analyses based on crack tip geometry in Fig. 3. The number of valence electrons per atom is 6.0 for pure W, and it decreases/increases linearly with increasing concentration of Ta/Re. (a) The variations of critical stress intensity factor K_{Ic} for Griffith cleavage and K_{Ie} for dislocation emissions of both $\frac{1}{2}\langle 111\rangle\{\bar{2}11\}$ and $\frac{1}{2}\langle 111\rangle\{\bar{1}10\}$ slip systems. (b) The variations of the ductility parameter $K_{\mathrm{Ie}}/K_{\mathrm{Ic}}$ for both slip systems.

On the other hand, Fig. 15(b) also unveils that, when a small amount of Ta (less than 25%) is added to pure W, $K_{\mathrm{Ie}}/K_{\mathrm{Ic}}$ first increases to some extent for both $\frac{1}{2}\langle 111\rangle\{\bar{2}11\}$ and $\frac{1}{2}\langle 111\rangle\{\bar{1}10\}$ slip systems. These changes demonstrate that to slightly decrease valence electrons of W inhibits the dislocation emission near the crack tip under mode I loading along $\langle 100\rangle$ so that $W_{1-x}Ta_x$ VCA alloys prefer more brittle deformation. This result matches the previous DFT calculations [9] and experiments [5], both of which show that Ta reduces the ductility of W alloys when Ta concentration is smaller than 10%. However, when Ta concentration is higher than a specific value between 25% and 50%, $K_{\mathrm{Ie}}/K_{\mathrm{Ic}}$ of both slip systems for $W_{1-x}Ta_x$ VCA alloys decline to values smaller than their counterparts of pure W. These W alloys with high Ta concentration become more ductile compared with pure W, consistent with the elastic shear instability (ESI) revealed by ideal tensile calculations in Sec. III B 1.

Another interesting result of these LEFM analyses is the change of the preferable slip system in W alloys. A comparison of K_{Ie} between two slip systems in Fig. 15(a) indicates that the $\frac{1}{2}\langle 111\rangle\{\bar{2}11\}$ slip system is more favorable for the dislocation emission at the crack tip than $\frac{1}{2}\langle 111\rangle\{\bar{1}10\}$ in pure W and W-Re alloys, but adding a significant amount (∼50%) of Ta solutes into W generates a preference to $\frac{1}{2}\langle 111\rangle\{\bar{1}10\}$ dislocation emission. This transformation of the preferable slip system by the variation of valence electrons is consistent with our phonon analyses in $W_{1-x}Ta_x$ and $W_{1-x}Re_x$ VCA alloys as shown in Figs. 11 and 12. It also agrees with the results of DFT-based dislocation core structure calculations and microcantilever bending experiments [10], which show that adding Re in W facilitates the $\frac{1}{2}\langle 111\rangle\{\bar{2}11\}$ dislocations while alloying Ta in W favors the $\frac{1}{2}\langle 111\rangle\{\bar{1}10\}$ dislocations.

IV. CONCLUSION

Tuning the d-band filling by chemical alloying can make the brittle bcc W metal more ductile due to different lattice instability mechanisms [23]. Similarly to pure W, W-Ta alloys with small Ta concentration prefer brittle cleavage fracture during [100] ideal tensile deformation so that they are still intrinsically brittle. The addition of high-concentration (∼50%) Ta makes elastic shear instability occur before brittle cleavage fracture during [100] ideal tensile deformation so that these W-Ta alloys are intrinsically ductile. Consistently, LEFM analyses reveal that a small amount of Ta (less than ∼25%) in W-Ta alloys increases their preference of {100} cleavage fracture propagation over dislocation emissions near the crack tip under mode I loading along ⟨100⟩, so these W-Ta alloys should be more brittle than pure W. Higher Ta concentrations (above a specific value between 25% and 50%) in W-Ta alloys induce the preference of dislocation emissions, especially for those of $\frac{1}{2}\langle 111\rangle\{\bar{1}10\}$ slip systems, so these W-Ta alloys should be intrinsically ductile.

Re inhibits elastic shear instability in W-Re alloys during [100] ideal tensile deformation. However, Re above a critical concentration (∼25%) in W-Re alloys provokes the phonon instability with the $T_{[2\bar{1}1]}[2\xi\ \xi\ \bar{\xi}]$ phonon mode before the W-Re alloys reach the elastic tensile instability. The propagation of this unstable phonon mode should correspond to the initialization of $\frac{1}{2}[1\bar{1}1](21\bar{1})$ dislocation nucleation, so these W-Re alloys are still intrinsically ductile. Consistently, LEFM analyses show that, when Re concentration is above a similar critical concentration, the emission of dislocations in the $\frac{1}{2}\langle 111\rangle\{\bar{2}11\}$ slip system is mostly more favorable than {100} cleavage fracture propagation and $\frac{1}{2}\langle 111\rangle\{\bar{1}10\}$ dislocation emission near the crack tip under mode I loading along ⟨100⟩, so these W-Re alloys should be intrinsically ductile also according to LEFM analyses.

Three different criteria, elastic instability of perfect crystals under ideal tensile deformation, phonon instability of the same perfect crystals, and LEFM analyses of crack tips under mode I loading, have been applied to evaluate the intrinsic ductility of W alloys in this work. The elastic and phonon instability criteria emphasize the aspect of stress/strain evolutions, and LEFM theory emphasizes the aspect of energetic variations. Because all of them are related to the nucleation of deformation defects (dislocations or cracks), consistent results on ductility evaluation of W alloys are obtained by these three methods as summarized above. Meanwhile, another criterion has been widely used to evaluate the ductility change for bcc metals based on the variation of the mobility of screw dislocations, which usually have lower mobility than the edge dislocations and control the plastic deformation in bcc metals [2,6–10]. In reality, both the dislocation nucleation and dislocation mobility can be essential to generate plastic deformation and determine the ductility depending on the detailed conditions. For example, it was found that the dislocation nucleation should be the limiting factor of the fracture behavior of W at low temperatures (around and below room temperature), while dislocation mobility should play more important roles at intermediate temperatures (∼400 K) [30].

For these reasons, to quantitatively evaluate the ductility and other mechanical properties of the real materials, it requires larger scale simulations to study the defect evolution and consider other factors, such as microstructures, temperature, and loading conditions. For example, recent experimental studies show that the ductility of W-Ta alloys is a complex function of Ta concentrations and microstructures (W-Ta solid solutions vs W-Ta composites with separate phases) [5,58]. In addition, whether and how strongly the shear/lattice instability modes under uniaxial tension are related to the intrinsic ductility depends on the detailed material systems. For example, martensitic transformation induced by shear instability increases the fracture toughness in ceramics [59]. However, the extent of the increasing toughness is limited by the finite strain provided by the martensitic transformation. On the other hand, the shear strain generated by dislocations is much higher to enhance the ductility. In general, for the bcc refractory metals and alloys, the differences in ductility behaviors found in the real materials indeed are consistent with the differences in their lattice instability behavior founded in this work [1,60]. These lattice instability criteria provide valuable and easily obtainable indicators of material ductility without considering other factors at a larger scale or from the external environment.

ACKNOWLEDGMENTS

C.M.Y. and Q.L. acknowledge support by startup funding from the University of Michigan, and this research was supported in part through computational resources and services provided by Advanced Research Computing at the University of Michigan, Ann Arbor.

[1] S. Zinkle and N. Ghoniem, Fusion Eng. Des. **51-52**, 55 (2000).

[2] L. Romaner, C. Ambrosch-Draxl, and R. Pippan, Phys. Rev. Lett. **104**, 195503 (2010).

[3] K. Einarsdotter, B. Sadigh, G. Grimvall, and V. Ozoliņš, Phys. Rev. Lett. **79**, 2073 (1997).

[4] P. Gumbsch, J. Riedle, A. Hartmaier, and H. F. Fischmeister, Science **282**, 1293 (1998).

[5] S. Wurster, B. Gludovatz, A. Hoffmann, and R. Pippan, J. Nucl. Mater. **413**, 166 (2011).
[6] D. R. Trinkle and C. Woodward, Science **310**, 1665 (2005).
[7] N. I. Medvedeva, Y. N. Gornostyrev, and A. J. Freeman, Phys. Rev. B **72**, 134107 (2005).
[8] N. I. Medvedeva, Y. N. Gornostyrev, and A. J. Freeman, Phys. Rev. B **76**, 212104 (2007).
[9] H. Li, C. Draxl, S. Wurster, R. Pippan, and L. Romaner, Phys. Rev. B **95**, 094114 (2017).
[10] H. Li, S. Wurster, C. Motz, L. Romaner, C. Ambrosch-Draxl, and R. Pippan, Acta Mater. **60**, 748 (2012).
[11] A. S. Argon, Acta Metall. **35**, 185 (1987).
[12] J. R. Rice, J. Mech. Phys. Solids **40**, 239 (1992).
[13] Y. Sun and G. E. Beltz, J. Mech. Phys. Solids **42**, 1905 (1994).
[14] S. J. Zhou, A. E. Carlsson, and R. Thomson, Phys. Rev. Lett. **72**, 852 (1994).
[15] J. Knap and K. Sieradzki, Phys. Rev. Lett. **82**, 1700 (1999).
[16] Z. Wu and W. Curtin, Acta Mater. **88**, 1 (2015).
[17] P. Andric and W. Curtin, J. Mech. Phys. Solids **106**, 315 (2017).
[18] D. Roundy, C. R. Krenn, M. L. Cohen, and J. W. Morris, Philos. Mag. A **81**, 1725 (2001).
[19] S. Giusepponi and M. Celino, J. Nucl. Mater. **435**, 52 (2013).
[20] A. Kelly and N. H. MacMillan, *Strong Solids* (Clarendon Press, Oxford, 1986).
[21] G. Grimvall, B. Magyari-Köpe, V. Ozoliņš, and K. A. Persson, Rev. Mod. Phys. **84**, 945 (2012).
[22] M. Šob, L. G. Wang, and V. Vitek, Mater. Sci. Eng., A **234**, 1075 (1997).
[23] L. Qi and D. C. Chrzan, Phys. Rev. Lett. **112**, 115503 (2014).
[24] W. Luo, D. Roundy, M. L. Cohen, and J. W. Morris, Jr., Phys. Rev. B **66**, 094110 (2002).
[25] N. Nagasako, M. Jahnatek, R. Asahi, and J. Hafner, Phys. Rev. B **81**, 094108 (2010).
[26] D. Hull, P. Beardmore, and A. Valintine, Philos. Mag. **12**, 1021 (1965).
[27] S. Kohlhoff, P. Gumbsch, and H. Fischmeister, Philos. Mag. A **64**, 851 (1991).
[28] J. Riedle, P. Gumbsch, and H. F. Fischmeister, Phys. Rev. Lett. **76**, 3594 (1996).
[29] F. Milstein and S. Chantasiriwan, Phys. Rev. B **58**, 6006 (1998).
[30] P. Gumbsch, J. Nucl. Mater. **323**, 304 (2003).
[31] S. Lee and R. Hoffmann, J. Am. Chem. Soc. **124**, 4811 (2002).
[32] K. Persson, M. Ekman, and G. Grimvall, Phys. Rev. B **60**, 9999 (1999).
[33] K. Persson, M. Ekman, and V. Ozoliņš, Phys. Rev. B **61**, 11221 (2000).
[34] D. M. Clatterbuck, C. R. Krenn, M. L. Cohen, and J. W. Morris, Phys. Rev. Lett. **91**, 135501 (2003).
[35] J. Li, A. H. Ngan, and P. Gumbsch, Acta Mater. **51**, 5711 (2003).
[36] A. A. Griffith, Philos. Trans. R. Soc., A **221**, 163 (1921).
[37] M. J. Mehl, D. A. Papaconstantopoulos, N. Kioussis, and M. Herbranson, Phys. Rev. B **61**, 4894 (2000).
[38] E. B. Tadmor and N. Bernstein, J. Mech. Phys. Solids **52**, 2507 (2004).
[39] S. Kibey, J. B. Liu, D. D. Johnson, and H. Sehitoglu, Acta Mater. **55**, 6843 (2007).
[40] M. de Jong, J. Kacher, M. H. F. Sluiter, L. Qi, D. L. Olmsted, A. van de Walle, J. W. Morris, Jr., A. M. Minor, and M. Asta, Phys. Rev. Lett. **115**, 065501 (2015).
[41] M. de Jong, L. Qi, D. L. Olmsted, A. van de Walle, and M. Asta, Phys. Rev. B **93**, 094101 (2016).
[42] G. Kresse and J. Furthmüller, Phys. Rev. B **54**, 11169 (1996).
[43] P. Giannozzi, S. Baroni, N. Bonini, M. Calandra, R. Car, C. Cavazzoni, D. Ceresoli, G. L. Chiarotti, M. Cococcioni, I. Dabo, A. Dal Corso, S. de Gironcoli, S. Fabris, G. Fratesi, R. Gebauer, U. Gerstmann, C. Gougoussis, A. Kokalj, M. Lazzeri, L. Martin-Samos, N. Marzari, F. Mauri, R. Mazzarello, S. Paolini, A. Pasquarello, L. Paulatto, C. Sbraccia, S. Scandolo, G. Sclauzero, A. P. Seitsonen, A. Smogunov, P. Umari, and R. M. Wentzcovitch, J. Phys.: Condens. Matter **21**, 395502 (2009).
[44] G. Kresse and D. Joubert, Phys. Rev. B **59**, 1758 (1999).
[45] J. Perdew, J. Chevary, S. Vosko, K. Jackson, M. Pederson, D. Singh, and C. Fiolhais, Phys. Rev. B **48**, 4978 (1993).
[46] H. J. Monkhorst and J. D. Pack, Phys. Rev. B **13**, 5188 (1976).
[47] M. Methfessel and A. T. Paxton, Phys. Rev. B **40**, 3616 (1989).
[48] A. Togo and I. Tanaka, Scr. Mater. **108**, 1 (2015).
[49] N. Troullier and J. L. Martins, Phys. Rev. B **43**, 1993 (1991).
[50] J. P. Perdew, K. Burke, and M. Ernzerhof, Phys. Rev. Lett. **77**, 3865 (1996).
[51] M. Fuchs and M. Scheffler, Comput. Phys. Commun. **119**, 67 (1999).
[52] S. Baroni, S. De Gironcoli, A. Dal Corso, and P. Giannozzi, Rev. Mod. Phys. **73**, 515 (2001).
[53] V. Vitek, Philos. Mag. **18**, 773 (1968).
[54] A. Stroh, Philos. Mag. **3**, 625 (1958).
[55] R. A. Ayres, G. W. Shannette, and D. F. Stein, J. Appl. Phys. **46**, 1526 (1975).
[56] H. A. Jahn and E. Teller, Proc. R. Soc. London, Ser. A **161**, 220 (1937).
[57] M.-C. Marinica, L. Ventelon, M. Gilbert, L. Proville, S. Dudarev, J. Marian, G. Bencteux, and F. Willaime, J. Phys.: Condens. Matter **25**, 395502 (2013).
[58] E. Tejado, P. A. Carvalho, A. Munoz, M. Dias, J. B. Correia, U. V. Mardolcar, and J. Y. Pastor, J. Nucl. Mater. **467**, 949 (2015).
[59] R. H. J. Hannink, P. M. Kelly, and B. C. Muddle, J. Amer. Ceramic Soc. **83**, 461 (2000).
[60] M. El-Genk and J. Tournier, J. Nucl. Mater. **340**, 93 (2005).